Dynamic Thermal Analysis of DFIG Rotor-side Converter during Balanced Grid Fault

Zhou, Dao; Blaabjerg, Frede

Published in:
Proceedings of the 2014 IEEE Energy Conversion Congress and Exposition (ECCE)

DOI (link to publication from Publisher):
10.1109/ECCE.2014.6953821

Publication date:
2014

Dynamic Thermal Analysis of DFIG Rotor-side Converter during Balanced Grid Fault

Dao Zhou, Frede Blaabjerg
Department of Energy Technology
Aalborg University
Aalborg, Denmark
zda@et.aau.dk; fbl@et.aau.dk

***Abstract*—Ride-through capabilities of the Doubly-Fed Induction Generator (DFIG) during grid fault have been studied a lot. However, the thermal performance of the power device during this transient period is seldom investigated. In this paper, the DFIG performance in terms of the stator flux evolution and the rotor voltage during the balanced grid fault is firstly addressed. By using the traditional demagnetizing control, the damping of the stator flux and the safety operation area are theoretically evaluated with various amounts of demagnetizing current. It is observed that the higher demagnetizing current leads to faster stator flux damping and lower induced rotor voltage, but it brings higher loss as well as the thermal cycling of the power device. Based on the simulation of the stator flux evolution and the thermal behavior of each power semiconductor, it is concluded that there is a trade-off in selection of the demagnetizing current coefficient, and it should be jointly decided by the suitable transient period and reliable operation of the power device.**

I. INTRODUCTION

The Doubly-Fed Induction Generator (DFIG) is a widely used configuration for wind turbines above 1 MW [1], [2]. It provides the advantage of variable speed operation and four-quadrant active and reactive power capabilities using the converter for only a small fraction (20%-30%) of the rated power. However, on detecting a grid fault, the generator unit is usually disconnected to protect the vulnerable rotor converter. In the recent years, this has been achieved by a so-called crowbar. As the penetration of wind power continues to increase, more wind turbines are required to ride through the grid faults, and to contribute to the system stability after the fault clearance. Researchers are addressing this issue from several points of view. For instance, the study described in [3], [4] analyzes the intrinsic in the DFIG during the grid fault and proposes its dynamic model. Many control strategies are suggested to support the DFIG to ride through the grid fault without the crowbar or with the enable time of the crowbar as soon as possible [5], [6]. The thermal behavior of the power devices during grid fault is evaluated for both the permanent-magnet synchronous generator full-scale based power converter and the DFIG partial-scale based power converter at steady-state operation [7].

This paper focuses on studying the transient thermal behavior of the DFIG wind turbine system during the balanced grid fault, in order to identify critical issues which can cause lifetime reduction. Section II is a brief introduction to the performance of the DFIG during balanced grid fault, and then by using the demagnetizing control, the influence of rotor current on the stator flux damping and the rotor terminal voltage is analyzed and simulated in section III. The power loss and thermal profile of the switching power device with various amounts of demagnetizing current are shown in Section IV. Finally, conclusions are drawn in the last section.

II. FLUX EVOLUTION OF DFIG UNDER BALANCED GRID FAULT

A large number of papers have discussed the ride-through operation of the wind turbine system with DFIG. As shown in Fig. 1, additional hardware - crowbar and dc chopper are basically employed for the DFIG wind power converter to overcome the severe grid fault [4], [8], [9].

If a balanced grid fault occurs on the terminal of the wind turbine system, as the stator flux cannot be changed abruptly, a stator natural flux ψ_{sn} will be introduced, and it is a dc component with respect to the stator winding, decaying with the time constant τ_s, as expressed in (1) [4],

$$\psi_{sn} = p \cdot \frac{U_s}{j\omega_0} \cdot e^{-\frac{t}{\tau_s}} \tag{1}$$

where p denotes the voltage dip level, U_s denotes the original stator voltage, ω_0 denotes the synchronous speed. This freezing stator natural flux introduces a large Electro-Motive Force (EMF) in respect to the rotor winding, and it may lead to an overvoltage or overcurrent of the Rotor-Side Converter (RSC). Moreover, the typical time constant of stator flux for the MW induction generator, which is decided by the ratio of the stator inductance L_s and stator resistance R_s, is normally several seconds [4]. As a consequence, it could be difficult for the RSC to ride through the fault duration without any help from advanced control scheme or hardware protection.

978-1-4799-5776-7/14/$31.00 ©2014 IEEE

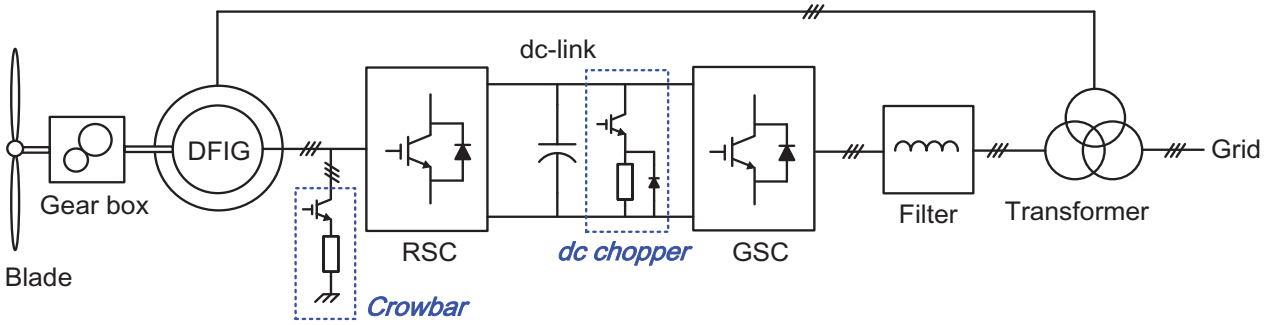

Fig. 1. Doubly-Fed Induction Generator (DFIG) wind turbine system for Low Voltage Ride-Through (LVRT) with both a crowbar and a dc chopper. (GSC: Grid-side converter; RSC: Rotor-side converter).

Meanwhile, the remaining grid voltage introduces a stator forced flux ψ_{sf}, which is rotating with the grid frequency.

$$\psi_{sf} = (1-p)\cdot\frac{U_s}{j\omega_0}\cdot e^{j\omega_0 t} \tag{2}$$

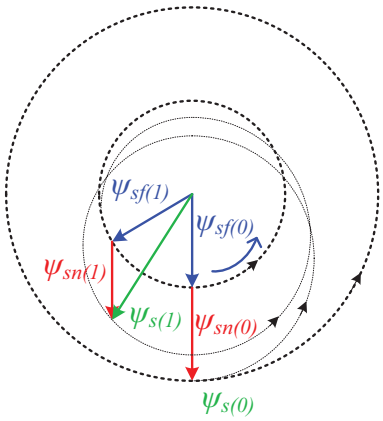

Fig. 2. Transient stator flux evolution in case of the balanced grid dip.

The transient stator flux evolution is then shown in Fig. 2. At the moment of the grid fault occurrence, the original flux $\psi_{s(0)}$ divides into the nature flux $\psi_{sn(0)}$ and the forced flux $\psi_{sf(0)}$. During the period of the grid fault, the amplitude of the rotating forced flux remains the same from $\psi_{sf(0)}$ to $\psi_{sf(1)}$, while the freezing natural flux exponentially decreases from $\psi_{sn(0)}$ to $\psi_{sn(1)}$. Eventually, the final evolution of the stator flux becomes a smaller circle compared to the original stator flux evolution.

III. Control Scheme during Balanced Grid Fault

As the objective of the RSC is to obtain variable rotor voltages through the control of the rotor current, the influence of the rotor current on the stator flux decaying and the rotor terminal voltage will be analyzed in this section.

As studied in [4], according to the natural machine model, the stator flux can be expressed in terms of the rotor current,

$$\frac{d}{dt}\psi_{sn} = -\frac{R_s}{L_s}\psi_{sn} + \frac{R_s}{L_s}L_m i_r \tag{3}$$

It is evident that the decaying of the stator flux can be either accelerated or decelerated with different directions of the rotor current in respect to the stator natural flux. Meanwhile, based on the modern grid codes [10], the reactive current is preferred as soon as possible, implying that the DFIG should have small decaying time constant of the stator natural flux in order to eliminate the transient period quickly.

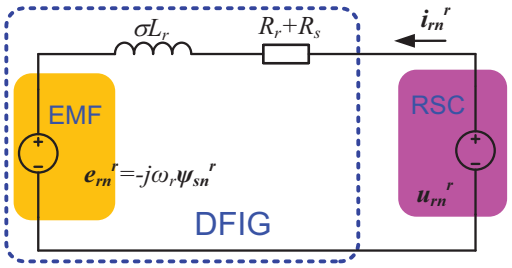

Fig. 3. Single-phases equivalent machine model in viewpoint of the rotor.

As the RSC is performed as a boost converter, the induced voltage at the rotor terminal is generally less than the dc-link voltage. Consequently, if the rotor terminal voltage is too high, the RSC will be out of control, and the uncontrolled rotor current may destroy the power switching device of the RSC.

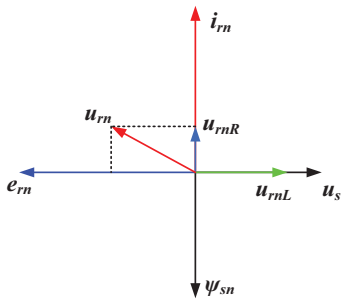

Fig. 4. Space vector diagram of the rotor voltage in the rotor reference frame.

As discussed in [11] and shown in Fig. 3, the rotor terminal voltage in rotor reference frame is jointly decided by the voltage drop of the combined stator and rotor resistance (u_{rnR}), the rotor transient inductance σL_r (u_{rnL}) as well as the EMF introduced by the stator natural flux (e_{rn}). Assuming the grid voltage is the reference vector, Fig. 4 graphically shows the space vector diagram of the rotor voltage, where the stator flux is lagging the stator voltage 90 degree, and the rotor current is opposite to the stator flux. As a result, the rotor voltage can be calculated as,

$$u_r^r = \omega_r(\sigma L_r i_r^r - \psi_{sn}^r) + j(R_r + R_s)i_r^r \quad (4)$$

where the ω_r denotes the rotor speed, and the superscript r denotes the value in the rotor reference frame. It is observed that the direction of the rotor current in respect to the stator natural flux is also closely related to the induced rotor voltage.

TABLE I. GENERATOR SPECIFICATION

Rated power	2 MW
Operational range of rotor speed	1050-1800 rpm
Rated amplitude of stator phase voltage	563 V
Rated frequency	50 Hz
Stator resistance	1.69 mΩ
Rotor resistance	1.52 mΩ
Mutual inductance	2.91 mH
Stator leakage inductance	0.04 mH
Rotor leakage inductance	0.06 mH
Ratio of stator winding and rotor winding	0.369

TABLE II. ROTOR-SIDE CONVERTER SPECIFICATION

Rated power	400 kW
Rated amplitude of rotor phase current	915 A
Rated amplitude of rotor phase voltage	305 V
DC-link capacitor	20 mF
DC-link voltage	1050 V
Used power module in each arm	1 kA/1.7 kV; two in parallel

Xiang *et al.* [3] proposed the demagnetizing control technique to protect the rotor converter against the grid fault without a crowbar or with a reduced crowbar enable time. The basic idea of the demagnetizing control is to keep the rotor current in the opposite direction of the stator natural flux,

$$i_{rn} = -k\psi_{sn} \quad (5)$$

A case study is carried on with a 2 MW DFIG wind turbine system, whose relevant parameters are summarized in TABLE I and TABLE II. Substituting (5) and (1) into (3), the decaying time constant of the stator natural flux can be calculated in terms of the rotor current,

$$\tau = \frac{L_s}{R_s} \cdot \frac{1}{1 + \frac{L_m \cdot \omega_0}{pU_s} \cdot i_{rn}} \quad (6)$$

where i_{rn} is the rated amplitude of the rotor phase current.

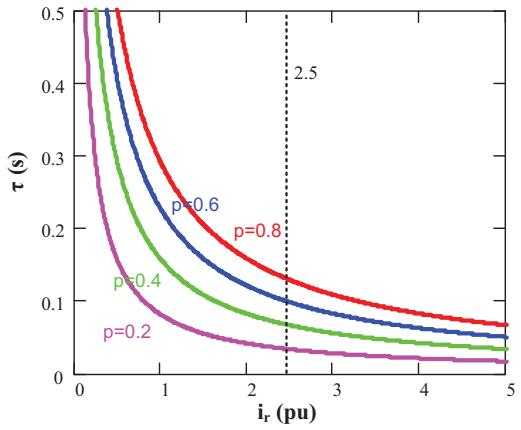

Fig. 5. The demagnetizing current effects on stator flux decaying with various voltage dip levels.

If the demagnetizing coefficient is expressed in terms of the rotor current (in pu value), the time constant of the decaying stator flux is only related to the voltage dip level p, as shown in Fig. 5. It is noted that the same amount of the demagnetizing current leads to different time constants of the stator natural flux at various voltage dips. Furthermore, it can be seen that, in case of the same voltage dip, the higher demagnetizing current results in shorter period of the stator natural flux.

On the other hand, the safety operation area can be expressed in terms of the rotor current by substituting (5) into (4),

$$\left|u_r^r\right| = \left|\omega_r(\sigma L_r i_r^r - \frac{pU_s}{\omega_0}) + j(R_r + R_s)i_r^r\right| \quad (7)$$

It is noted that the rotor voltage is related to both the voltage dip level p and the rotor speed ω_r. Three rotor speeds 1050 rpm, 1500 rpm and 1800 rpm are selected to represent the sub-synchronous, synchronous and super-synchronous of the DFIG, and their safety operation area are shown in Fig. 6. Due to the power device capacity as well as the rated rotor current and voltage listed in TABLE II, it is evident that the RSC can support up to 2.5 pu rotor current. Moreover, if the full modulation index is assumed, 1050 V DC-link voltage is transformed at 2.0 pu rotor voltage. Assuming the 1.7 kV power device can endure 2.0 kV voltage stress for a short period, then 4.0 pu rotor voltage is regarded as the limitation of the voltage stress. As shown in Fig. 6, it can be seen that higher voltage dip introduces larger rotor voltage, which is consistent with (7). Moreover, if the suitable amount of the demagnetizing current is chosen, the RSC is able to ride through the grid fault at voltage dip up to 0.8.

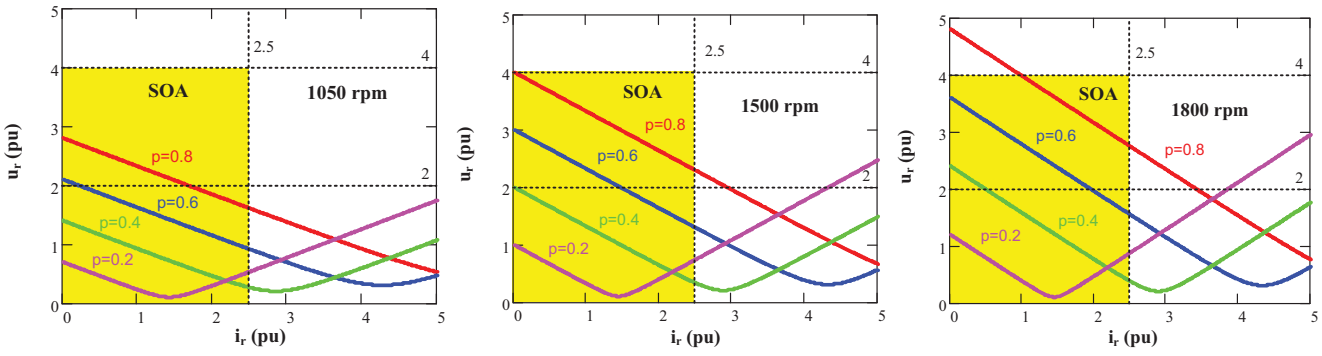

Fig. 6. The demagnetizing current effects on rotor terminal voltage with various voltage dip levels. (a) Rotor speed at 1050 rpm; (b) Rotor speed at 1500 rpm; (c) Rotor speed at 1800 rpm.

As shown in Fig. 7, in the case of the occurrence or clearance of the grid fault, the control strategy switches from the conventional vector control to the demagnetizing control. Moreover, the stator flux is obtained through the flux observer, in which a band-pass filter is applied to separate the stator natural flux from the total stator flux. Various demagnetizing current are realized by the different selections of the demagnetizing coefficient *k*.

If the dip level of 0.8 balanced grid fault occurs at the moment of 0.5 second, the simulated results with different amounts of the demagnetizing current are shown in Fig. 8, in which the different rotor speeds are also taken into account. As shown in Fig. 8(a) and Fig. 8(b), in case of the same rotor speed, it is noted that the stator flux becomes stable sooner if higher demagnetizing current is provided, which is consistent with decaying time of the stator flux calculated in (6). Meanwhile, if 0.5 pu demagnetizing current is supplied, the required rotor voltage as well as the DC-link voltage is higher than 2.5 pu demagnetizing current due to its higher voltage drop across the transient inductor to counteract the induced EMF as analyzed in (7). However, if 2.5 pu demagnetizing current is selected, the amplitude of rotor current becomes higher, implying the more stressed power device.

If the different rotor speeds are considered, as shown in Fig. 8(b) and Fig. 8(c), same amount of the demagnetizing current leads to the same decaying time of the stator flux. However, the required rotor voltage and DC-link voltage is smaller at lower rotor speed because the lower rotor speed causes lower EMF as analyzed in (7). Furthermore, as the fluctuation of the electromagnetic torque is closely related to the reliability of the mechanical part, it is also presented in the simulation result.

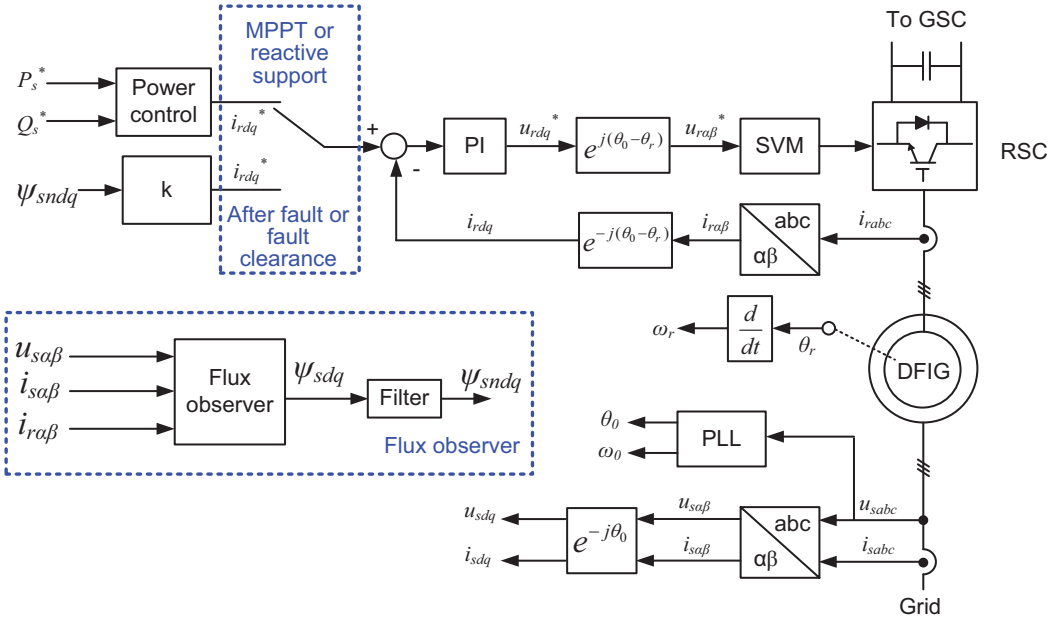

Fig. 7. Control schemes of vector control and demagnetizing control in case of the grid fault.

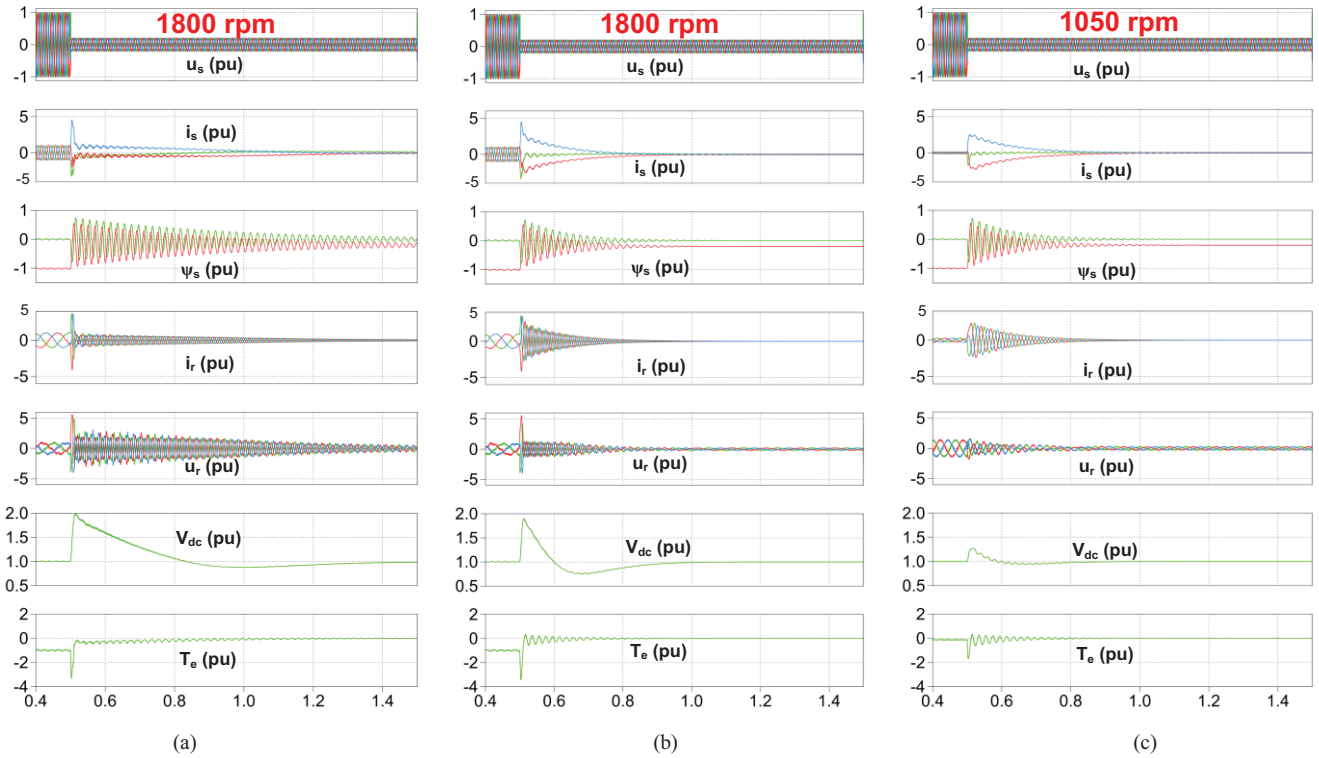

Fig. 8. Simulation results with different amounts of the demagnetizing current at various rotor speeds. (a) 0.5 pu demagnetizing current if rotor speed is 1800 rpm; (b) 2.5 pu demagnetizing current if the rotor speed is 1800 rpm; (c) 2.5 pu demagnetizing current if the rotor speed is 1050 rpm.

IV. Loading of Power Device with Various Control Schemes

As analyzed in Section III, the amount of the demagnetizing current should be as large as possible from both the stator flux and the induced rotor voltage point of view. However, the maximum amount of the demagnetizing current extremely stresses the power semiconductors. As a consequence, there may be a trade-off between the damping time of the stator flux and the loading of the power devices.

A. Power loss of power device

The power loss model, consisting of the conduction losses and switching losses, can be referred to [7]. Based on the on-state voltage drop and switching energy against the load current and the DC-link voltage provided by the manufacturers, the conduction losses and switching losses are accumulated by every switching cycle within one fundamental frequency. Consequently, the simulation of the power loss has been obtained with the use of PLECS blockset in Simulink [12].

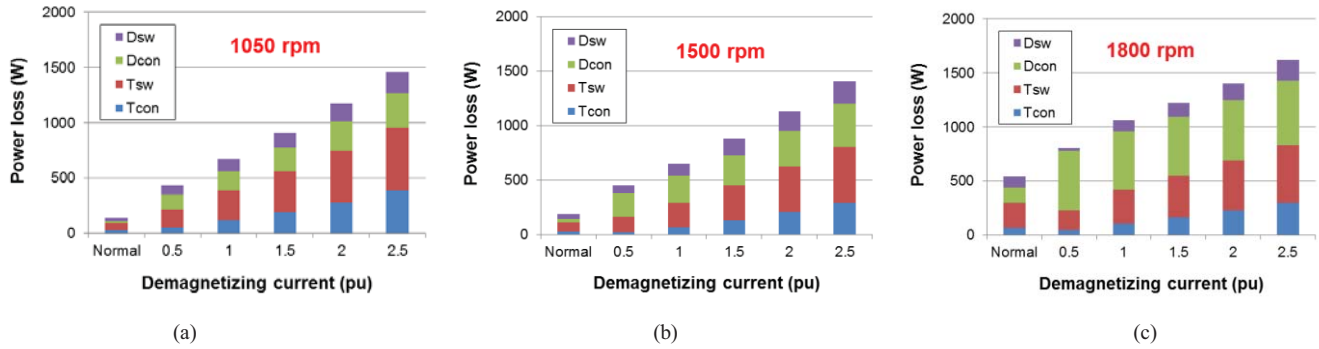

Fig. 9. Loss distribution of the power devices at different rotor speeds in terms of various demagnetizing currents. (a) 1050 rpm; (b) 1500 rpm; (c) 1800 rpm.

As shown in Fig. 9, the various amounts of the demagnetizing current are considered at different rotor speeds. Before the grid fault happens, due to the Maximum Power Point Tracking (MPPT), it is noted that the higher rotor speed makes the power device more stressed. Moreover, as the DFIG absorbs or produces the active power

to the RSC in the sub-synchronous mode or the super-synchronous mode, it indicates that the more conduction loss of the IGBT is dissipated in the sub-synchronous mode, while the more conduction loss of the diode is consumed in the super-synchronous mode. If the grid fault occurs, as the demagnetizing control tries to absorb the reactive power through the RSC, it inevitably changes the loading of the power semiconductor devices compared to normal vector control. Moreover, it can be seen that, regardless of the rotor speed, the more amount of the demagnetizing current results in heavier loading of the power device.

B. Thermal behavior of power device

A thermal impedance that decides the junction temperature of the common power device mainly consists of the thermal parameters of the power module itself (from junction to baseplate or case), and the thermal parameters of the Thermal Integrate Material (TIM) and cooling method. It can be given either in a Cauer structure (physical model) or a Foster structure (mathematical model). The thermal impedance inside the power module is usually tested by the power semiconductor manufacturer, and the value is provided in terms of multi-layer Foster structure, as listed in TABLE III. As the cooling methods depend on the users' different applications, the thermal impedance of the heat-sink is basically not included in the power semiconductor manufacturer datasheet. However, it can normally be provided from the cooling manufacturer.

TABLE III. JUNCTION TO CASE THERMAL IMPEDANCE OF POWER MODULE

		1st	2nd	3rd	4th
IGBT	R (ºC/kW)	0.3	1.6	18	3.1
	τ (s)	0.0003	0.0013	0.04	0.4
Diode	R (ºC/kW)	0.48	3.61	34.6	6.47
	τ (s)	0.0002	0.0009	0.03	0.2

Fig. 10 shows a thermal model that combines the power module and cooling thermal impedance. Generally, the thermal time constant of typical air cooling is from dozens of seconds to hundreds of seconds for MW-level power converter, while the maximum thermal time constant of power device is hundreds of milliseconds. On the other hand, the maximum fundamental period of the RSC output current is only one second, which implies that the thermal cycling induced by the cooling method can almost be neglected [7].

As a result, for the dynamic thermal analysis, the thermal model of cooling is simply regarded as the controlled voltage source, and it will not disturb with the junction temperature fluctuation due to huge difference between the fault transient time (hundreds of milliseconds) and thermal constant of typical cooling method.

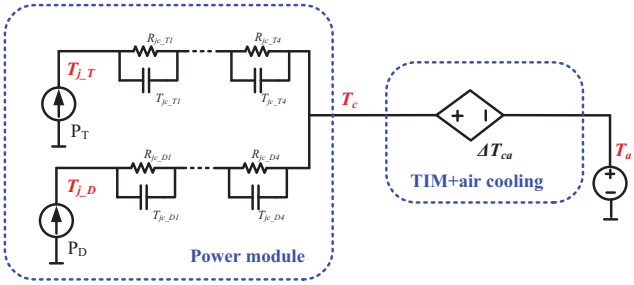

Fig. 10. Thermal model of the power switching semiconductor.

With the thermal model implemented in PLECS, the thermal performance of the power device can then be simulated as shown in Fig. 11. It is worth to mention that the junction temperature excursion is highly dependent on response time of the current controller, as the current reference in *dq* rotating frame during the demagnetizing control becomes sinusoidal signal other than dc component of the vector control.

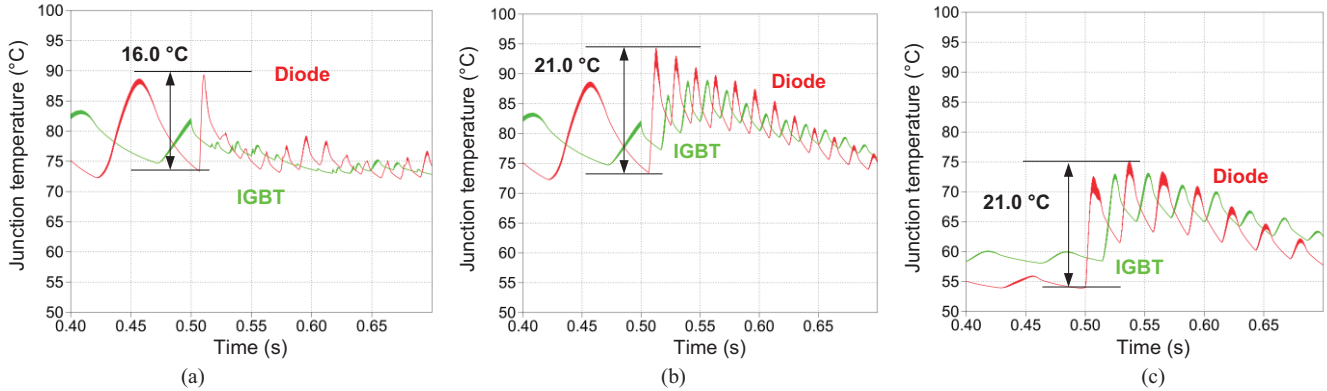

Fig. 11. Junction temperature at various amounts of demagnetizing current as well as the different rotor speeds. (a) 0.5 pu demagnetizing current if rotor speed is 1800 rpm; (b) 2.5 pu demagnetizing current if the rotor speed is 1800 rpm; (c) 2.5 pu demagnetizing current if the rotor speed is 1050 rpm.

In the case of rotor speed at 1800 rpm, before the grid fault happens, the diode is more stressed than the IGBT with junction temperature fluctuation of 15.3 ºC. During the occurrence of the grid fault, if 0.5 pu demagnetizing current is preferred as shown in Fig. 11(a), the diode becomes a little more stressed 16.0 ºC, while the IGBT relieves slightly. If 2.5 pu demagnetizing current is provided as shown in Fig. 11(b), both the IGBT and the diode are more stressed than

the normal operation, in which the diode has 21.0 ºC maximum junction temperature fluctuation. In the case of the rotor speed at 1050 rpm, if 2.5 pu demagnetizing current is provided as shown in Fig. 11(c), both the IGBT and the freewheeling diode are much more stressed, and the maximum thermal cycling of changes from 2.1 ºC to 21.0 ºC during the grid faults. It is noted that, although the current through the power device reaches its rated value at 2.5 pu demagnetizing current, the junction temperature is still not so high, even below 100 ºC. The reason is that, during such a short period of the 2.5 pu current (dozens of milliseconds as shown in Fig. 11), the junction temperature is not able to react so fast due to the thermal time constant inside the power module (hundreds of milliseconds in TABLE III).

In order to evaluate the thermal profile of the power device with different amounts of demagnetizing current, Fig. 12 summarizes the junction temperature at voltage dip level at 0.8 with rotor speeds 1050 rpm, 1500 rpm and 1800 rpm, respectively. It is noted that the diode is more stressed than the IGBT by using demagnetizing control, and the junction temperature variation increases with higher amount the demagnetizing current. Moreover, regardless of the rotor speed, the same amount of the demagnetizing control causes the similar junction temperature fluctuation.

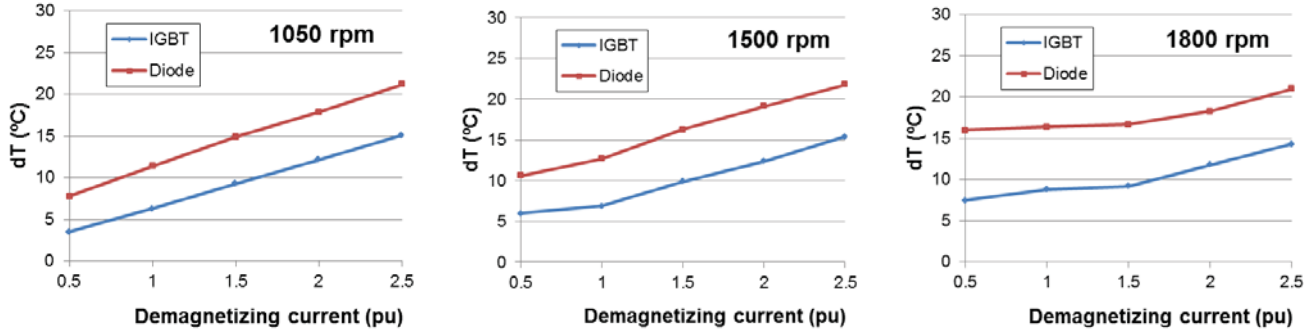

(a) (b) (c)

Fig. 12. Compariosn of the junction temperature variation at different rotor speeds with various amounts of the demagnetizing current. (a) 1050 rpm; (b) 1500 rpm; (c) 1800 rpm.

V. CONCLUSION

This paper has addressed the DFIG performance in terms of the stator flux evolution and the rotor voltage during the balanced grid fault. By using the demagnetizing control, the damping of the stator flux and the safety operation area is theoretically evaluated with various amounts of demagnetizing current. It is observed that the higher demagnetizing current leads to faster stator flux damping and lower induced rotor voltage, but it brings higher loss as well as the thermal cycling of the power device. Based on the simulated power loss and thermal cycling of each power semiconductor, it is concluded that there is a trade-off in selection of the demagnetizing current coefficient, and it should be jointly decided by the suitable transient period and reliable operation of the power device.

REFERENCES

[1] F. Blaabjerg, K. Ma, "Future on power electronics for wind turbine systems," *IEEE Journal of Emerging and Selected Topics in Power Electronics*, vol. 1, no. 3, pp. 139-152, Sep. 2013.

[2] H. Polinder, J. A. Ferreira, B. B. Jensen, A. B. Abrahamsen, K. Atallah, R. A. McMahon, "Trends in wind turbine generator systems," *IEEE Journal of Emerging and Selected Topics in Power Electronics*, vol. 1, no. 3, pp. 174-185, Sep. 2013.

[3] D. Xiang, L. Ran, P. J. Tavner, S. Yang, "Control of a doubly fed induction generator in a wind turbine during grid fault ride-through," *IEEE Trans. on Energy Conversion*, vol. 21, no. 3, pp. 652-662, Sep. 2006.

[4] J. Lopez, E. Gubia, E. Olea, J. Ruiz, L. Marroyo, "Ride through of wind turbines with doubly fed induction generator under symmetrical voltage dips," *IEEE Trans. on Industrial Electronics*, vol. 56, no. 10, pp. 4246-4254, Oct. 2009.

[5] W. Chen, D. Xu, M. Chen, F. Blaabjerg, "Comparison of current control strategies for DFIG under symmetrical grid voltage dips," *in Proc. of IECON 2013*, pp. 1540-1545, Nov. 2013.

[6] S. Xiao, G. Yang, H. Zhou, H. Geng, "An LVRT control strategy based on flux linkage tracking for DFIG-based WECS," *IEEE Trans. on Industrial Electronics*, vol. 60, no. 7, pp. 2820-2832, July 2013.

[7] D. Zhou, F. Blaabjerg, M. Lau, M. Tonnes, "Thermal analysis of two-level wind power converter under symmetrical grid fault," *in Proc. of IECON 2013*, pp. 1902-1907, Nov. 2013.

[8] I. Erlich, H. Wrede, C. Feltes, "Dynamic behavior of DFIG-based wind turbines during grid faults," *in Proc. of PCC 2007*, pp. 1195-1200, Apr. 2007.

[9] B. Gong, D. Xu, B. Wu, "Cost effective method for DFIG fault ride-through during symmetrical voltage dip," *in Proc. of IECON 2010*, pp. 3269-3274, Nov. 2010.

[10] E.ON-Netz. Requirements for offshore grid connections, Apr. 2008.

[11] G. Abad, J. Lopez, M. Rodriguez, L. Marroyo, G. Iwanski, Doubly fed induction machine-modeling and control for wind energy generation. Piscataway, NJ: IEEE Press, 2011, pp. 265-302.

[12] User manual of PLECS blockset version 3.2.7 March 2011. (Available: http://www.plexim.com/files/plecsmanual.pdf.